LIMNOLOGY
and
OCEANOGRAPHY: METHODS

ASLO

Limnol. Oceanogr.: Methods 17, 2019, 223–239

doi: 10.1002/lom3.10307

A new numerical model for understanding free and dissolved gas progression toward the atmosphere in aquatic methane seepage systems

Pär Jansson,[1]* **Bénédicte Ferré**,[1] **Anna Silyakova**,[1] **Knut Ola Dølven**,[1] **Anders Omstedt**[2]

[1]Department of Geosciences, CAGE-Centre for Arctic Gas Hydrate, Environment and Climate, UiT the Arctic University of Norway, Tromsø, Norway

[2]Department of Marine Sciences, University of Gothenburg, Gothenburg, Sweden

Abstract

We present a marine two-phase gas model in one dimension (M2PG1) resolving interaction between the free and dissolved gas phases and the gas propagation toward the atmosphere in aquatic environments. The motivation for the model development was to improve the understanding of benthic methane seepage impact on aquatic environments and its effect on atmospheric greenhouse gas composition. Rising, dissolution, and exsolution of a wide size-range of bubbles comprising several gas species are modeled simultaneously with the evolution of the aqueous gas concentrations. A model sensitivity analysis elucidates the relative importance of process parameterizations and environmental effects on the gas behavior. The parameterization of transfer velocity across bubble rims has the greatest influence on the resulting gas distribution, and bubble sizes are critical for predicting the fate of emitted bubble gas. High salinity increases the rise height of bubbles; whereas temperature does not significantly alter it. Vertical mixing and aerobic oxidation play insignificant roles in environments where advection is important. The model, applied in an Arctic Ocean methane seepage location, showed good agreement with acoustically derived bubble rise heights and in situ sampled methane concentration profiles. Coupled with numerical ocean circulation and biogeochemical models, M2PG1 could predict the impact of benthic methane emissions on the marine environment and the atmosphere on long time scales and large spatial scales. Because of its flexibility, M2PG1 can be applied in a wide variety of environmental settings and future M2PG1 applications may include gas leakage from seafloor installations and bubble injection by wave action.

The importance of natural and anthropogenic methane (CH_4) emissions to the atmosphere has been increasingly recognized in the last few decades as CH_4 contributes to greenhouse warming by about 20% (Edenhofer et al. 2014; Pachauri et al. 2014), because CH_4 is 32 times more potent than CO_2 in terms of warming potential (Pachauri et al. 2014).

Large CH_4 reservoirs in the form of hydrates, a crystalline structure comprising water molecules encapsulating guest molecules such as CO_2 and hydrocarbons (Sloan and Koh 2007), exist in sediments along continental margins worldwide. They are presently estimated to contain 1800 Gt of carbon (Ruppel and Kessler 2016), equivalent to one sixth of the global mobile carbon pool. Hydrates are stable under high pressure and low temperature, suggesting that bottom water warming potentially dissociates hydrates at the boundary of their stability (Westbrook et al. 2009). Yearly global flux of CH_4 to the atmosphere associated with dissociation of hydrate deposits is presently estimated at 6 Tg, which amounts to less than 1% of the total CH_4 flux to the atmosphere (Kirschke et al. 2013), but hydrate dissociation rates may increase as ocean bottom water temperatures increase over human time scales (Ferré et al. 2012).

A substantial amount of CH_4 is also found trapped where permafrost (water ice that is frozen all year) caps exist. Gaseous CH_4 trapped under hydrate and permafrost caps is presently released through the water column and to the atmosphere on the East Siberian Shelf as the caps become more and more permeable as a result of thawing (Shakhova et al. 2010). In the light of a rapidly warming Arctic Ocean, it is therefore crucial to understand the transport mechanisms of

*Correspondence: per.g.jansson@uit.no

Additional Supporting Information may be found in the online version of this article.

CH_4 from the seabed through the water column and potentially to the atmosphere in order to estimate the impacts of seafloor CH_4 emissions on the climate and the environment.

CH_4 in sediments may be present as hydrates, free (bubbles) and/or dissolved gas in pore water. CH_4 percolating upward is subject to anaerobic oxidation within the sulfate–methane transition zone (Boetius and Wenzhöfer 2013), but in high-velocity fluid flow systems, both dissolved CH_4 and bubbles can bypass this filter (Luff et al. 2004; Panieri et al. 2017).

After being released from the seafloor, most of the CH_4 contained in bubbles dissolve in the water column as the bubbles ascend toward the sea surface. Numerical bubble models predict that gas exchange occurs across the bubble rims and a majority of the CH_4 initially present within the bubbles dissolve near the seafloor (Leifer and Patro 2002; McGinnis et al. 2006). Subsequently, dissolved CH_4 diffuses, is advected by ocean currents away from its source, and is at least partly oxidized in the presence of methanotrophic bacteria (Damm et al. 2005; Uhlig and Loose 2017). Biastoch et al. (2011) modeled the effect of microbial CH_4 oxidation on ocean acidification and showed that the ocean pH could decrease by as much as 0.25 units in a 100-yr period in some areas of the Arctic Ocean. At shallow water depths, bubbles may transport CH_4 to the upper mixed layer of the ocean, where the now-dissolved CH_4 may be ejected to the atmosphere by diffusive equilibration. Shakhova et al. (2014) reported a significant reduction of dissolved CH_4 concentration in the water column on the shallow East Siberian Arctic Shelf (water depth < 50 m) directly after two storm events, suggesting that diffusive emission of CH_4 to the atmosphere was enhanced by the strong vertical mixing induced by the storms. However, large CH_4 emissions from the seafloor at a slightly deeper site (~ 90 m) west of Svalbard in the summer of 2014 did not contribute to increased CH_4 concentration in the atmosphere (Myhre et al. 2016). Although the acoustic signature of bubble streams was observed to reach close to the sea surface, only traces of the high CH_4 concentration near the seafloor was observed near the surface. This effect was attributed to efficient gas exchange across bubble rims, and the presence of a pycnocline was suggested to inhibit vertical turbulent transport of dissolved CH_4 toward the sea surface and atmosphere.

The motivation for this study was to improve the understanding of the role of the hydrosphere in locations where CH_4 is leaking from the seafloor. Specifically, the vertical distribution of free and aqueous CH_4 is of great interest in order to assess potential CH_4 release to the atmosphere and biochemical changes in the aquatic habitat.

In order to predict the fate of CH_4 or any other kind of gas, contained in bubbles in the water column, it is necessary to consider interaction with other kinds of existent gas. Only simultaneous consideration of bubble dissolution and evolution of dissolved gas can allow for understanding these processes and their impact. Briefly, as bubbles rise through the water column, gas of all present species may diffuse across the bubble rims. If the aqueous concentration of a gas species is higher (or lower) than the equilibrium concentration, predicted by the mixing ratio of the corresponding gas inside the bubble, gas of this species will invade (or evade) the bubble. As they rise, bubbles grow or shrink at rates depending on the gas transfer and ambient pressure change. This implies that fluxes of different gas species affect each other in an intricate system, and it is therefore imperative to simultaneously model free and dissolved gases as well as bubble sizes, shapes, and rising speeds.

Numerical bubble models have been developed previously, but each show limitations. Delnoij et al. (1997) developed a bubble model for a gas–liquid column, which resolves bubble–bubble interaction (bouncing and coalescence) but does not take into account gas dissolution or pressure gradients. Johansen (2000) modeled nonideal gas behavior but ignored ambient dissolved gas and only modeled CH_4. Leifer and Patro (2002) introduced a bubble model based on empirical observations of bubble rising speeds but assumed spherical bubbles and ignored the nonideal behavior of gases due to pressure and temperature. McGinnis et al. (2006) provided a bubble model resolving five bubble gases, nitrogen (N_2), oxygen (O_2), carbon dioxide (CO_2), methane (CH_4), and argon (Ar) but did not couple free and dissolved gas and did not consider multiple bubble sizes. Stepanenko et al. (2011) presented a natural process-based model for shallow lakes with the production of CH_4 in the sediment, assuming immediate escape of CH_4 to the atmosphere. Liang et al. (2011) presented a near-surface coupled bubble and dissolved gas model but used a size spectrum of bubbles ranging from 0 to only 0.8 mm, adequately assuming spherical bubbles. Vielstädte et al. (2015) developed a linearized single-bubble model with three gas species (N_2, O_2, and CH_4) for the North Sea, which is only valid for depths shallower than 100 m and ignores the evolution of dissolved gases.

All of the above models depend on parameterizations of gas, water, and bubble properties and so uncertainties associated with those are abundant. The objective of this study is to develop and verify a new numerical model, filling knowledge gaps of previous models. The major improvements of the marine two-phase gas model in one dimension (M2PG1) presented here, over previous bubble models are:

1. Dissolution (gas escaping the bubble) and exsolution (gas invading the bubble) to simulate the evolution of the free gas composition of several gas species inside the bubbles.
2. Coupling of the dissolution and exsolution of bubble gas to the temporal evolution of the dissolved gas concentration in the water column.
3. Bubbles of different sizes and size-dependent shapes.
4. Nonideal gas behavior for changing temperature and pressure within the bubbles as they rise through the water column.
5. Calculation of pressure-, salinity-, and temperature-dependent solubility of five gas species (N_2, O_2, CO_2, CH_4, and Ar).
6. Gas emission of free gas and equilibration of dissolved gas with the atmosphere.

7. Coupling with existing models, resolving transport and diffusion of water properties is made possible because of the structure of the model.

To our knowledge, M2PG1 is the first model that is able to simulate free and dissolved gas simultaneously, while using multiple bubble sizes and several gas species in both free and dissolved phases. Nonideal gas compressibility, environment-dependent solubility, and diffusivity are included in the model as well as interaction with the atmosphere of the free and dissolved phase of all included gas species. This study focuses on CH_4 seepage from the seafloor in a cold (Arctic Ocean) environment. We aim to elucidate on the relative importance of the process parameterizations and compare the effects of environmental conditions on the gas dynamics. We describe the model setup and detail the process parametrizations and subsequently present a sensitivity analysis, comparing the importance of parameterizations of rising speed, bubble shapes, and gas transfer with the importance of bubble sizes, temperature, salinity, CH_4 oxidation rates, dissolved gas concentrations, turbulent vertical mixing, and water currents. The model was applied to a known CH_4 seep site west of Svalbard (e.g., Westbrook et al. 2009; Sahling et al. 2014), and a comparison between model results and acquired data is presented.

Method

M2PG1 simulates the evolution of free gas (bubbles) rising through the water column while resolving interaction with dissolved gas and the ultimate exchange of gas with the atmosphere via direct bubble transport and/or equilibration with atmospheric gas species. The model incorporates pressure-, temperature-, and salinity-dependent gas compressibility, solubility, and diffusivity and simulates multigas and multisize bubbles with user-defined initial gas composition and user-defined bubble size distribution (BSD). Bubbles can be released at any chosen water depth within the domain. This study focuses on the evolution of free and dissolved gases occurring after gas (CH_4) bubbles are released from the seafloor and interaction with atmospheric and dissolved N_2, O_2, CO_2, CH_4, and Ar. The following sections describe how M2PG1 models these processes.

Model implementation

We implemented M2PG1 in PROBE, a well-documented and freely available numerical equation solver (Svensson 1978; Omstedt 2011) using a finite volume discretization and FORTRAN. PROBE has been successfully used for prediction of growth and melting of sea ice (Omstedt and Wettlaufer 1992), coupling between weather forecasting and a process-based ocean model (Gustafsson et al. 1998), frazil ice dynamics (Svensson and Omstedt 1998), marine climate studies (Hansson and Omstedt 2008), the effect of wave-dependent momentum flux (Carlsson et al. 2009), and the carbonate system in the Baltic Sea (Edman and Omstedt 2013). The equation solver supports a process-based approach and is intended for numerical representation of the environment and to test and build new system understanding. It is well suited for climate impact studies, resolving the vertical structure of the investigated properties of the water column. PROBE solves the conservation equations (Eq. 1) for the state variables, ϕ, which in this study are salinity, temperature, and dissolved gas species (N_2, O_2, CO_2, CH_4, and Ar).

$$\frac{\partial \phi}{\partial t} + \frac{Q_{IN} - Q_{OUT}}{A} \times \frac{\partial \phi}{\partial z} = \frac{\partial}{\partial z}\left(\Gamma_\phi \frac{\partial \phi}{\partial z}\right) + \theta^\phi \quad (1)$$

The first term $\left(\frac{\partial \phi}{\partial t}\right)$ represents the local (at depth z) change with time of the state variable. The second term $\left(\frac{Q_{IN} - Q_{OUT}}{A} \times \frac{\partial \phi}{\partial z}\right)$ is the vertical advection given by multiplying the vertical gradient of the state variable by the volume convergence of inflow and outflow (Q_{IN} and Q_{OUT}) normalized by the domain area (A). The right-hand side shows diffusion $\left(\frac{\partial}{\partial z}\left(\Gamma_\phi \frac{\partial \phi}{\partial z}\right)\right)$ and local source/sink terms (θ^ϕ). The salinity, temperature, and concentration of dissolved gas species are represented on a vertical finite volume grid. The free gas is represented in an identical vertical grid and in bubble size classes with equivalent radii ($[r - \delta r/2, r + \delta r/2]$).

Free gas (bubbles) rises through the water column at speeds mainly dependent on bubble size and shape, while the exchange of gases across the bubble rims alters the gas composition and concentration inside and outside the bubble. While previous seawater bubble models (e.g., Leifer and Patro 2002; McGinnis et al. 2006; Vielstädte et al. 2015) were Lagrangian, i.e., simulating the evolution of a single bubble, M2PG1 uses a Eulerian, vertically oriented finite volume grid and a bubble size spectrum to simulate any number and sizes of bubbles simultaneously. This requires that bubble rising and shrinking or growing are discretized. The processes involved are shown in Fig. 1 together with the numerical grid, where light blue indicates dissolved gas and yellow indicates free gas. Temperature and salinity are omitted in the figure for clarity. The model is integrated (moved forward in time) using the Euler method, resolving all the above-described processes simultaneously.

Coupled conservation equations for free and dissolved gas

The processes constituting the source and sink terms in Eq. 1 can be summarized in a set of coupled conservation equations describing the temporal evolution of free gas content and dissolved gas concentration (Eqs. 2 and 3, where the superscript $j \in [N_2, O_2, CO_2, CH_4, Ar]$ denotes gas species and subscripts i and k indicate indices for depth and bubble size, respectively). Additional source/sink terms at the vertical and lateral domain boundaries are given in Eqs. 4 and 5. Notations are summarized in the Supporting Information S1, and each mathematical term in the equations are described in the following sections.

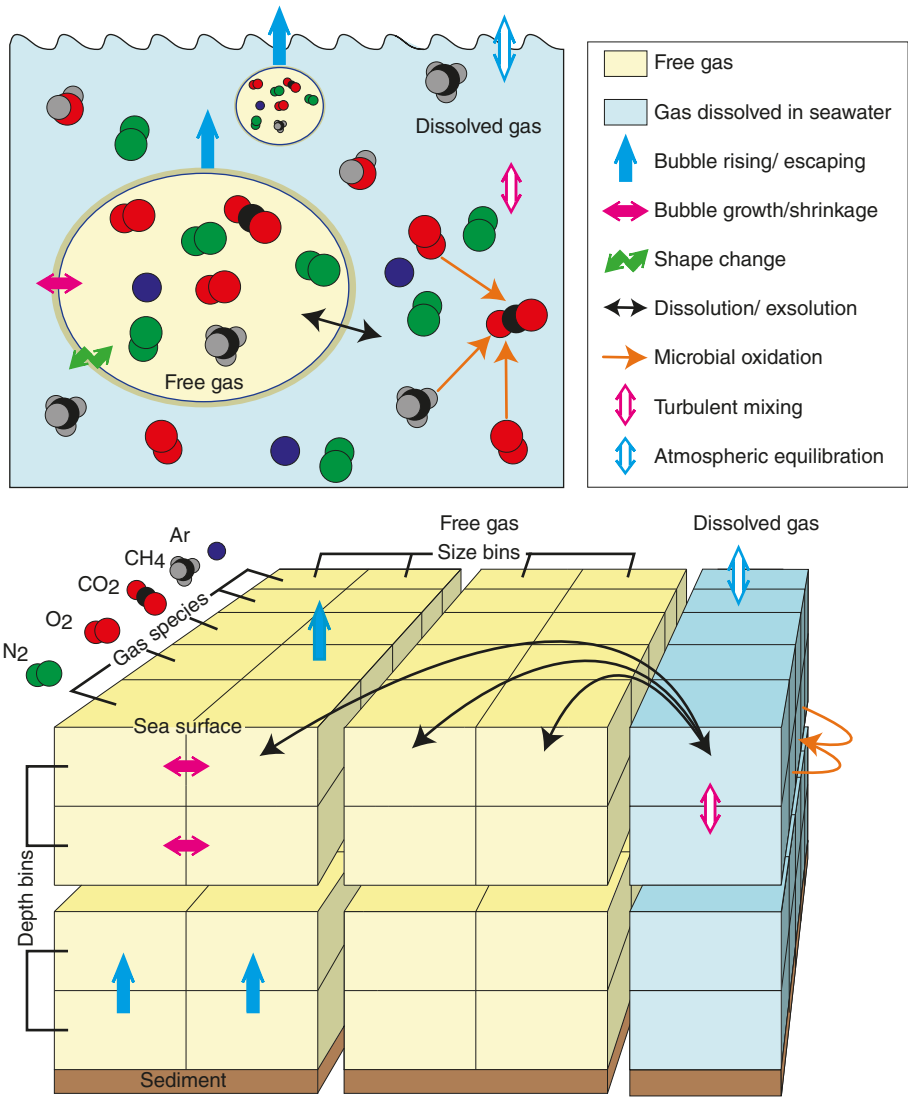

Fig. 1. Diagram illustrating the physical processes involved as gas bubbles rise through the water column. Upper panel: Schematic of the processes occurring in the water column (blue background) and in the bubbles (yellow background). The processes are denoted by arrows and described in the text. Lower panel: Representation of the numerical model setup and processes. The left part of the grid (yellow) shows the free gas contained in depth bins, bubble size bins, and gas species. The right part (blue) represents the dissolved gases in the corresponding depth and species grid. Process arrows in the lower panel appear as in the upper panel. For sketch simplicity, only examples of the processes are drawn (e.g., bubble rising potentially occurs between all depth bins and growth/shrinkage occurs between all size bins).

$$\frac{\partial n^j_{i,k}}{\partial t} = \frac{\partial n^j_{\mathrm{R}_{i,k}}}{\partial t} + \frac{\partial n^j_{\mathrm{D}_{i,k}}}{\partial t} \tag{2}$$

$$\theta^j_i = -\left(\frac{\sum_{k=1}^{k=\mathrm{NSBIN}} \partial n^j_{\mathrm{D},k}/\partial t}{[\rho_{\mathrm{SW}} \times A \times \delta_z]} \right)_i + S_{\mathrm{OX}}(i,j) \tag{3}$$

In Eq. 2, $\frac{\partial n_{\mathrm{R}}}{\partial t}$ is the temporal evolution of free gas due to rising bubbles as visualized in Fig. 2a and quantified in the section Rising Bubbles. $\frac{\partial n_{\mathrm{D}}}{\partial t}$ is the free gas evolution due to bubble-dissolution visualized in Fig. 2b and detailed in the section Exchange of Free and Dissolved Gas Across Bubble Rims. In Eq. 3, $\left(\frac{\sum_{k=1}^{k=\mathrm{NSBIN}} \partial n^j_{\mathrm{D},k}/\partial t}{[\rho_{\mathrm{SW}} \times A \times \delta_z]} \right)_i$ is the dissolved gas concentration change corresponding to the dissolution occurring in all bubble sizes. The second term, S_{OX} represents the sources and sinks resulting from aerobic CH_4 oxidation as illustrated in Fig. 1 and quantified in the section Aerobic Oxidation of CH_4. Free gas content and dissolved gas concentrations are integrated forward in time simultaneously with temperature and

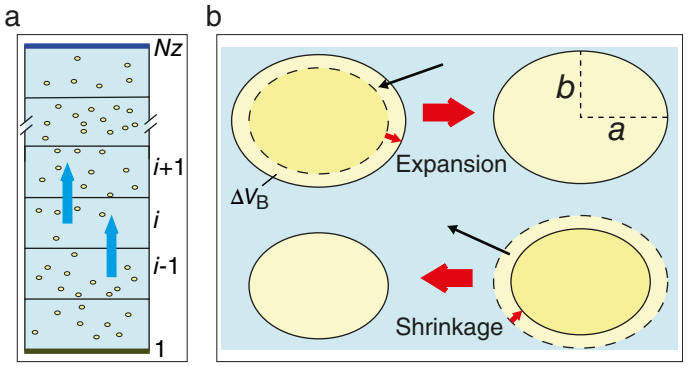

Fig. 2. Representation of bubbles rising, expanding, and shrinking. **(a)** Vertical grid with indices starting from 1 at the seafloor and up toward the surface bin, *N*. Ellipses illustrate bubbles within each depth bin and blue arrows indicate bubbles rising to the current bin from below and rising up to the next higher bin. **(b)** Bubbles shrinking or expanding as described in the text. The volumetric difference between bubbles in adjacent size bins is indicated by ΔV_B and small red arrows. Bubbles are assumed oblate spheroids. Here, *a* denotes the length of the horizontal (semimajor) axis, and *b* denotes the length of the vertical (semiminor) axis.

salinity, starting with initial conditions and forced by boundary conditions.

Initial- and boundary conditions

Supplementary to the local sources and sinks, free gas content and dissolved gas concentration are affected by fluxes across the domain boundaries. Equation 4 describes the source and sink terms of free gas at the vertical boundaries, and Eq. 5 describes the source and sink terms of dissolved gas at the lateral and vertical boundary. It is assumed that there is no dissolved gas emitted from the seafloor and no free gas is transported from beyond the lateral boundary.

$$\frac{\partial}{\partial t}\left(n^j_{i\in[\mathrm{bot,surf}],k}\right) = Q^j_{\mathrm{EF}_k} - Q^j_{\mathrm{AF}_k} \tag{4}$$

$$\theta^j_{\mathrm{B}_i} = Q_{\mathrm{IN}_i} \times C^j_{\mathrm{B}_i} - Q_{\mathrm{OUT}_i} \times C^j_{\mathrm{SW}} i - \left(\frac{Q^j_{\mathrm{AEQ}_i}}{\rho_{\mathrm{SW}_i} \times A_i \times \delta_{z_i}}\right)_{i=\mathrm{surf}} \tag{5}$$

In Eq. 4, Q_{EF} represents the flow rate of emitted free gas (here CH_4 bubbling from the seafloor) and Q_{AF} is the bubble gas escaping to the atmosphere from the sea surface. In Eq. 5, $\left(Q_{\mathrm{IN}_i} \times C^j_{\mathrm{B}_i} - Q_{\mathrm{OUT}_i} \times C_{\mathrm{SW}} i^j\right)_i$ is the concentration change due to the lateral transport of dissolved gas *j* in and out of the model domain. Q_{IN_i} and Q_{OUT_i} are the volumetric inflow and outflow, respectively, from the boundary at depth *z*(*i*), C_{B_i} is the concentration at the boundary, and C_{SW_i} is the concentration in the modeled water column. $\left(\frac{Q^j_{\mathrm{AEQ}}}{\rho_{\mathrm{SW}} \times \mathrm{A} \times \delta_z}\right)_{i=\mathrm{surf}}$ represents the concentration change due to equilibration of dissolved gas *j* with the atmosphere, where Q_{AEQ} is the amount of gas emitted per time unit, ρ_{SW} is the seawater density calculated from temperature and salinity according to Fofonoff (1985), and *A* and δ_z are the horizontal area and vertical extent of the model cell, respectively.

As bubble dynamics depend on temperature, salinity, and dissolved gas concentrations in the water column, initial and boundary conditions include vertical profiles of the modeled gas concentration and of temperature and salinity. Initial conditions are provided by the user with the same vertical resolution as the model grid (here, the profiles are 400 m with a 1-m resolution). M2PG1 can be forced with transient aquatic boundary conditions with vertical resolution matching the vertical grid of the forcing data and transient atmospheric boundary conditions can be specified. However, as the sensitivity analysis of this study aims at evaluating the influence of implemented parameters individually, we initiate the simulations with vertically homogenous profiles of dissolved gas, temperature and salinity. The case study, on the other hand, uses measured profiles of temperature, salinity, and oxygen. Gas species, other than oxygen, are expected to be in equilibrium with the atmosphere as we lack measurements of them. The structure of the user-specified initial and boundary conditions are listed in Supporting Information Table S7. All simulations in this study use static boundary conditions (temperature, salinity, and dissolved gases). The inflow and outflow of heat, salinity, and dissolved gas of different species are handled by PROBE's built-in functionality.

Rising bubbles

In order to evaluate the importance of bubble rising speed on the distribution of gas in the water column, M2PG1 includes different bubble rising speed models (BRSM) that the user can select (Supporting Information Table S2). Bubbles accelerate quickly after their emission and reach terminal velocity within milliseconds when the buoyancy and drag forces balance. We therefore assume that the bubble rising speed can be derived from ambient conditions and bubble sizes, and there is no need to simulate acceleration from the moment when bubbles are released from the seafloor. The rising of gas contained in bubbles of specific sizes is discretized as visualized in Fig. 2a. The first term on the right-hand side of Eq. 2 describes the rate of change with time of the content of a particular gas species at depth z(*i*) for each bubble size resulting from rising bubbles. This is quantified in Eq. 6, where w_b is the rising speed of the bubble.

$$\frac{\partial n_{\mathrm{R}i}}{\partial t} = \frac{w_{\mathrm{b}_{i-1}} \times n_{i-1}}{\delta z_{i-1}} - \frac{w_{\mathrm{b}_i} \times n_i}{\delta z_i} \tag{6}$$

Bubble hydrodynamics, and therefore, bubble rising speeds are influenced by surfactants on the bubble rims. Different surfactants such as bacteria (Blanchard 1989), ions (Collins et al. 1978), and oil (Leifer et al. 2000) may contribute to immobilization of the bubble rim and can change the rising speed of bubbles. The reference case uses the BRSM suggested by Woolf (1993), because, in spite of its simplicity, it considers both clean and surfactant-covered bubbles and because the

velocities are intermediate compared to other models over the relevant range of bubble sizes.

Exchange of free and dissolved gas across bubble rims

Transfer of gas molecules across bubble surfaces is a stochastic process, occurring continuously, and the net transfer is zero only when equilibrium between the free and the aqueous phase of all gas species arise simultaneously. Mass conservation requires that the sink of free gas in the bubbles, due to dissolution, $\frac{\partial n^j_{\mathrm{D}i,k}}{\partial t}$ in Eq. 2, is complemented by a source of dissolved gas (Eq. 3) in the water column. This is quantified by the transfer equation (e.g., Leifer and Patro 2002; McGinnis et al. 2006), giving the rate of change of bubble gas content resulting from dissolution/exsolution:

$$\frac{\partial n^j_{\mathrm{D}} i,k}{\partial t} = A_{\mathrm{BS}i,k} \times \rho_{\mathrm{SW}_i} \times k^j_{\mathrm{T}} i,k \times \left[C^j_{\mathrm{SW}} i,k - C^j_{\mathrm{EQ}} i,k \right] \tag{7}$$

In the following sections, the transfer velocity (k_{T} in Eq. 7) models (TVMs) and parameterizations of the surface area of bubbles (A_{BS}) are discussed. C_{EQ} is the dissolved gas concentration, which would result in equilibrium between the dissolved phase and the free gas inside the bubble. It is given by the solubility S and the molar fraction ($X = \frac{n^j}{\sum_1^{\mathrm{NGAS}} n^j}$) of gas species j in the bubble according to:

$$C^j_{\mathrm{EQ}} i,k = S^j_{i,k} X^j_{i,k} \tag{8}$$

The solubility of bubble gas in seawater depends on the total pressure inside the bubble and the temperature and salinity of the surrounding seawater and is specific for each gas species. The pressure inside a gas bubble is affected by the hydrostatic ($P_{\mathrm{H}}(z) = \int_z^0 \rho_{\mathrm{SW}} \times g \, dz$) and atmospheric ($P_{\mathrm{ATM}}$) pressures as well as the pressure induced by surface tension on the bubble interface (P_{ST_k}). The total pressure inside the bubble is given by: $P_{\mathrm{Bb}_{i,k}} = P_{\mathrm{H}_i} + P_{\mathrm{ATM}} + P_{\mathrm{ST}_k}$, where $P_{\mathrm{ST}_k} = 2\sigma / r_{\mathrm{E}k}$. Here, r_{E} is the equivalent bubble radius, and σ is the surface tension, taken as tension between air and water. M2PG1 uses the latest parameterizations of solubilities of the included gas species (Supporting Information Table S1) that are currently available in the literature (Supporting Information Table S1).

Gas transfer velocity

According to Eq. 5, the gas transfer across the bubble interface depends on the transfer velocity, k_{T}. Jähne et al. (1987) showed that k_{T} depends on the diffusion coefficient, the Schmidt number, the local small-scale turbulence, the temperature, and the surfactants potentially present on the bubble rim. Numerical simulations and empirical observations have been performed, but no observation of gas transfer rates has been conducted in the deep sea and so parameterizations of k_{T} in natural aquatic environments are not found in the literature. Consequently, M2PG1 allows for a number of TVMs that the user can choose from, similarly to the choice of BRSM. Presently, M2PG1 includes the transfer velocity parameterization of Zheng and Yapa (2002) for clean bubbles (TVM No. 1), parameterizations for semiclean (TVM No. 2), and surfactant-covered (TVM No. 3) bubbles (McGinnis et al. 2006). The transfer velocity is strongly dependent on the gas diffusivity for which we rely on parameterizations listed in Supporting Information Table S1. The reference case uses the clean bubble parameterization, because it produces profiles similar to observations, whereas the two other parameterizations retain gases inside the bubbles for too long. In other environmental settings, for example, where bubbles escape from oily sediments, it may be appropriate to use a TVM based on observations of surfactant-covered bubbles.

Surface areas of non-spherical bubbles

Mass transfer across the bubble rims critically depends on the surface area of bubbles (Eq. 5) and earlier bubble models (Leifer and Patro 2002; McGinnis et al. 2006) assumed spherical bubbles. However, it is known that larger bubbles (transition around 1 mm radius) most often have oblate-like shapes (e.g., Rehder et al. 2002; Leblond et al. 2014). M2PG1 includes two parameterizations of bubble flatness, $f \equiv a/b$, where a and b are the semimajor and semiminor axis, respectively (Fig. 2b). The first parameterization follows Leblond et al. (2014). The authors suggested that bubble flatness is a function of the semimajor axis length, and they found a logarithmic relation: $f = 0.45 + 1.4 \times \ln(a)$, with a in mm. This flatness parameterization is valid for $a > 1.48$ mm, while smaller bubbles are assumed spherical (blue solid line in Fig. 3a). We introduce a linear flatness parametrization: $f = 1 + 0.3064a$ (blue dashed line in Fig. 3a), incorporating bubbles of small to large sizes. The surface area of an oblate spheroid, $A_{\mathrm{BS}} = 2\pi a^2 + \frac{2\pi b^2}{\epsilon} \times \tanh^{-1}\epsilon$, where the eccentricity $\epsilon = \sqrt{1 - \frac{b^2}{a^2}}$ (Al Zaitone 2018).

The BSD is given as $r_{\mathrm{E}} = \sqrt[3]{a^2 \times b}$ (Sam et al. 1996), requiring that M2PG1 solves for the semimajor and semiminor axes during simulation start-up depending on the shape parameterization chosen by the user. The surface area of a flat bubble, relative to bubble volume, is larger than the surface area of a spherical bubble of the same volume (Fig. 3b).

Bubble shrinkage and expansion

Two processes affect bubble volumes simultaneously as bubbles rise through the water column: (a) gas invades or escapes bubbles depending on the dissolved gas concentrations and gas composition in the bubble. Dissolution and exsolution can occur simultaneously if the concentration of one or several gas species is supersaturated with respect to the free gas inside the bubble and another gas species is undersaturated. The bubble volume changes at rates matching the gas transfer of all gas species across the bubble rim, as indicated with black arrows in Figs. 1 and 2. This is quantified by

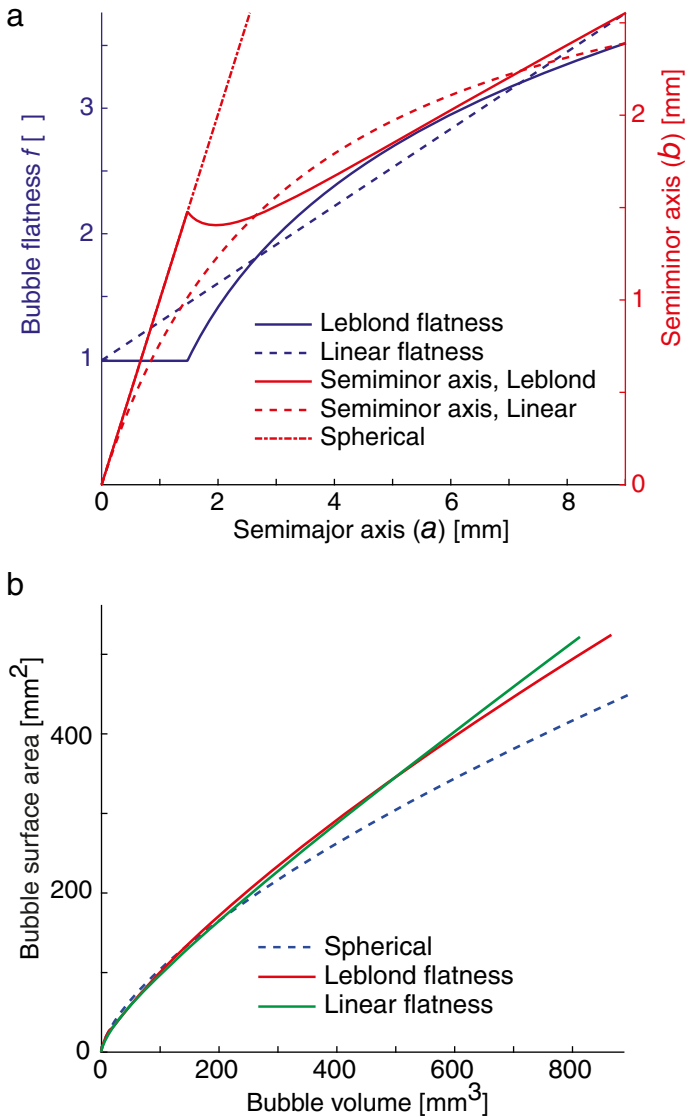

Fig. 3. Three parameterizations of bubble shapes. **(a)** The solid blue line indicates flatness as predicted by Leblond et al. (2014) dashed blue line represent the linear flatness. Red lines show the resulting semiminor axis as functions of semimajor axis for the case of spherical (dotted line), linear flatness (dashed, this study), and Leblond flatness (solid). **(b)** Surface area vs. bubble volume as calculated for the case of spherical bubbles (dashed blue), linear flatness (green, this study) and flatness according to Leblond (red).

$\frac{dV_D}{dt} = \sum_{j=1}^{NGAS} \frac{dn_{D_j}}{dt} \times V_{M_j}$, where V_M is the molar volume of the specific gas, calculated from ambient pressure and temperature, compliant with nonideal gas behavior and given by the parameterizations referenced in Supporting Information Table S1. (b) Rising bubbles experience pressure, temperature, and volume changes according to $\frac{dV_{PT}}{dt} = \sum_{j=1}^{NGAS} \frac{w_b n^j}{\delta z} \times \Delta V_M^j$. The total temporal volumetric rate of change of rising bubbles can be written for each bubble size at each depth:

$$\frac{dV}{dt} = \frac{dV_D}{dt} + \frac{dV_{PT}}{dt} \tag{9}$$

Discretizing this process, M2PG1 moves bubble gas between bubble sizes. When bubbles shrink ($dV/dt < 0$), the gas content of species j in bubble size $k - 1$ increases and the content in bubble size k will decrease with the same amount as seen in Eq. 10, where $\Delta V_B$is the volumetric difference between bubble sizes and X is the molar fraction of a particular gas species.

$$\frac{dn_{k-1}^j}{dt} = \frac{\frac{dV}{dt}}{\Delta V_B} \times \frac{V_k \times X^j}{V_M^j}$$
$$\frac{dn_{j,k}}{dt} = -\frac{\frac{dV}{dt}}{\Delta V_B} \times \frac{V_k \times X^j}{V_M^j} \tag{10}$$

When bubbles grow, gas moves from size k to size $k + 1$ in a similar manner. When the largest bubbles (k = NSBIN) are predicted to grow and smallest bubbles ($k = 1$) are predicted to shrink, the gas is retained in the present bin.

Aerobic oxidation of CH_4

Aerobic oxidation of CH_4 in the water column, a biogeochemical process described by the balanced chemical reaction equation $CH_4 + 2O_2 \Rightarrow CO_2 + 2H_2O$, implies a direct mathematical coupling between dissolved CH_4 and dissolved O_2 and CO_2. The oxidation process occurs at rates $\frac{\partial C^{CH_4}}{\partial t} = -k_{MOX} C^{CH_4}$ where k_{MOX} is the oxidation rate constant (time^{-1}) and C^{CH_4} is the CH_4 concentration (e.g., Graves et al. 2015). The stoichiometry depicts a 1 : 2 : 1 relation between the three gas species, yielding production rates of CO_2 equal to oxidation rates of CH_4 and twice as fast removal rates of O_2. Hence, the source and sink terms due to aerobic CH_4 oxidation in Eq. 3 become $\left[S_{OX_i}^{N_2} = 0;\ S_{OX_i}^{O_2} = -2k_{MOX} \times C_i^{CH_4};\ S_{OX_i}^{CO_2} = k_{MOX} \times C_i^{CH_4};\ S_{OX_i}^{CH_4} = -k_{MOX} \times C_i^{CH_4};\ S_{OX_i}^{Ar} = 0\right]$. k_{MOX} reported in the literature is typically between < 0.001 and 0.7 d^{-1} (Angelis and Scranton 1993; Valentine et al. 2001; Mau et al. 2017). The reference simulation uses a value of 0.01 d^{-1}, which is the average constant calculated by Graves et al. (2015) at the site of our case study. The amount of available O_2 sets a limitation on the CH_4 oxidation.

Turbulent vertical mixing

Dissolved gas in seawater, as well as heat content and salinity, are subject to vertical mixing by turbulent diffusion (e.g., Thorpe, 2007). The rate of change of the state variable (temperature, salinity, gas, or other) due to vertical diffusion is $\frac{\partial}{\partial z}\left(\Gamma \frac{\partial \phi}{\partial z}\right)$, where Γ is the vertical mixing coefficient, which can vary over several orders of magnitude. PROBE has the capability to either use a constant coefficient or calculate the coefficient according to turbulence closure schemes. Here, we apply a constant Γ in order to isolate the effect of vertical turbulent mixing and we assume that Γ is the same for all gas species.

Atmospheric interaction

Free gas can escape to the atmosphere if bubbles reach the sea surface as seen in Fig. 1. For this process, we simply assume that all bubbles reaching the surface *z* (*Nz*) immediately escape to the atmosphere. The flow of free gas of species *j* to the atmosphere is, therefore, $Q_{AB_j} = \sum_{k=1}^{NSBIN} n^j_{N,k}/\Delta t$, where Δt is the time step of the model simulation.

Furthermore, dissolved gases in the water column will equilibrate with the atmosphere. The flow rate to the atmosphere due to equilibration is calculated according to Wanninkhof (2014):

$Q^j_{AEQ} = A \times k^j_A \times \left(C^j_{Nz-1} - Ca^j\right)$, where $k^j_A\left(\mathrm{cm\,h^{-1}}\right) = 0.251 \times U^2 \times \left(\frac{Sc^j}{660}\right)^{-\frac{1}{2}}$, and *Sc* is the temperature-dependent Schmidt number, calculated for the different gas species according to Wanninkhof (1992) (Wanninkhof 2014) and *U* is the wind speed (m s^{-1}) 10 m above the sea surface. Positive rates indicate gas flow to the atmosphere.

User-specified simulation details

Environmental conditions controlling the evolution of free and dissolved gas are defined, and bubble shape parameterization, BRSM, and TVM are chosen by the user together with horizontal domain area, time step, interval for model output (detailed in Supporting Information Table S4), BSD (example in Supporting Information Table S5), composition of gas contained in emitted bubbles (Supporting Information Table S6), Q_{EF}, and k_{MOX}. The user can choose between constant or transient Γ (applied or calculated by the model). Transient oceanic and atmospheric boundary conditions can be used to force the model. All settings are supplied by the user in an initialization file, as detailed in Supporting Information Table S7.

Assessment

Budget analysis and numerical precision

The numerical precision of M2PG1 was assessed by simulating a 24 h continuous release of 0.1 mol CH_4 s^{-1} emitted at 80 m water depth as bubbles with initial r_E = 3 mm (linearly flat bubbles were assumed). The residual (*res*) was defined as the initial dissolved gas content plus the sources and sinks minus the integrated current free and dissolved gas content (Eq. 11). A smaller residual means better numerical precision.

$$res(t) = t = 0\overbrace{\sum_{i=2}^{Nz-1}\left(C^{CH_4}_{SW} \times \rho_W \times \delta z \times A\right)}^{t=0} + \sum_{t_m}^{t_m+\Delta t}\left[\left(Q_{EF} - Q_{AF} - Q_{AEQ} - \sum_{i=2}^{Nz-1} \mathrm{MOX}\right) \times \delta t\right] - t\overbrace{\sum_{i=2}^{Nz-1}\sum_{k=1}^{NSBIN} n_{i,k}}^{t} - t\overbrace{\sum_{i=2}^{Nz-1}\left(C^{CH_4}_{SW} \times \rho_W \times \delta_z \times A\right)}^{t} \quad (11)$$

Here, $t=0\overbrace{\sum_{i=2}^{Nz-1}\left(C^{CH_4}_{SW} \times \rho_W \times \delta z \times A\right)}^{t=0}$ represents the initial (t = 0) content of dissolved CH_4 and $t\overbrace{\sum_{i=2}^{Nz-1}\left(C^{CH_4}_{SW} \times \rho_W \times \delta_z \times A\right)}^{t}$ is the content at the time of the model output (every 10 min). The term $\sum_{t_m}^{t_m+\Delta t}\left[\left(Q_{EF} - Q_{AF} - Q_{AEQ} - \sum_{i=2}^{Nz-1}\mathrm{MOX}(i)\right) \times \delta t\right]$ represents the sources and sinks at the vertical boundaries: Q_{EF} is the free gas emission to the water column; Q_{AF} is the free gas emitted into the atmosphere; Q_{AEQ} is the dissolved gas escaping to the atmosphere by means of equilibration and MOX is the CH_4 removal by aerobic oxidation. These quantities are accumulated over time, written to result-files, and reset at time intervals of 10 min (Δt = 600 s) (t_m represents the time of the model output). The double summation $t\overbrace{\sum_{i=2}^{Nz-1}\sum_{k=1}^{NSBIN} n}^{t}$ represents the free gas CH_4 present at the current time where *n* represents the free gas molar content in bin *i, k*. *Nz* is the number of vertical grid cells and NSBIN is the number of bubble sizes. The residual was less than 1‰ of the total CH_4 gas content. Thus, the numerical accuracy was better than 99.9% for a 24 h test simulation.

Model sensitivity

The model sensitivity was analyzed with 53 simulations which were run to steady state, here identified when the relative integrated content difference between time steps was less than 10^{-6}. The sensitivity analysis was performed by separately evaluating bubble property parameterizations and environmental influence on the result. Analysis of different parametrizations and environmental conditions were further divided into subgroups consisting of a number of simulations as indicated in Table 1 and detailed in the Supporting Information Table S8. The reference case (M2PG1 0.0) uses BRSM No. 7, TVM No. 1, linearly flat bubbles, and vertically homogenous dissolved gas profiles at equilibrium with the atmosphere assuming atmospheric mixing ratios of 79% N_2, 20% O_2, 0.97% Ar, 399 ppm CO_2, and 1830 ppb CH_4, where ratios for CO_2 and CH_4 were obtained from the annual global average in 2015 (Ed Dlugokencky, NOAA/ESRL, www.esrl.noaa.gov/gmd/ccgg). It further uses a single BSD of 3 mm, which is the peak radius of the BSD observed by Veloso et al. (2015); a temperature of 4°C and a salinity of 35 PSU, which was observed near the seafloor during a cruise to the study area as described in the section Case Study; a flow rate of 0.05 mol s^{-1}, equivalent to the highest flow rate of observed bubble streams during the same cruise; a k_{MOX} of 0.01 d^{-1}, which is the mean, determined by Graves et al. (2015) in the same area; a water current of 15 cm s^{-1}, as determined from the typical inclination of bubble streams; Γ = 0.001 m^2 s^{-1}, was applied, which is high compared with sparse literature data from the area

(Randelhoff et al. 2015), but in the low range of oceanic values (Wunsch and Ferrari 2004).

Sensitivity to bubble property parameterizations

The sensitivity analysis of the bubble property parameterizations included simulations targeting bubble rising speeds and transfer velocities (Fig. 4) and a separate analysis of shape parameterizations. We compared the CH_4 profiles resulting from nine BRSMs (Supporting Information S2, Table S3, and Fig. S1). The existence of surfactants on the bubble rim and its effect on the rising speed is beyond the scope of this study, and the resulting profiles do not clearly discriminate between clean and surfactant-covered BRSMs. The transfer velocity parametrizations are coupled to the rising speed of bubbles, which implies that the analysis of BRSMs and TVMs are linked. For that reason, the effect of the choice of BRSMs remains unclear. However, studies suggest that bubbles observed in natural conditions behave as surfactant covered,

Table 1. Overview of simulations included in the sensitivity analysis.

	Subgroup	Target	Unit	Case settings
Bubble property parameterizations	1	Bubble rising speed	Model No.	1, 2, 3, 4, 5, 6, 7*, 8, 9
	2	Bubble shapes	Model	Spherical, Leblond, linear*
	3	Transfer velocity	Model No.	1*, 2, 3
Environmental settings	4	Dissolved gas profiles	μmol kg^{-1}	Atmospheric equilibrium*, half O_2, 1/100 O_2, no argon, double CO_2, no N_2, double N_2, 10-fold N_2
	5	BSD†	mm	1, 2, 3*, 4, 6, 8
	6	Temperature	°C	0‡, 1‡, 2‡, 3‡, 4*, 6, 8, 10, 20
	7	Salinity	PSU	0, 20, 35*, 40
	8	Flow rate	mol s^{-1}	0.025, 0.05*, 0.1, 0.2
	9	Oxidation rate constant	d^{-1}	0, 0.01*, 0.1, 1, 10
	10	Water current	m s^{-1}	0.025, 0.05, 0.1, 0.15*, 0.2, 0.5
	11	Mixing coefficient	m^2 s^{-1}	0.0001, 0.001*, 0.01, 1, 100, 10,000

*Used in reference case.
†Single initial bubble radius.
‡Within CH_4-HSZ.

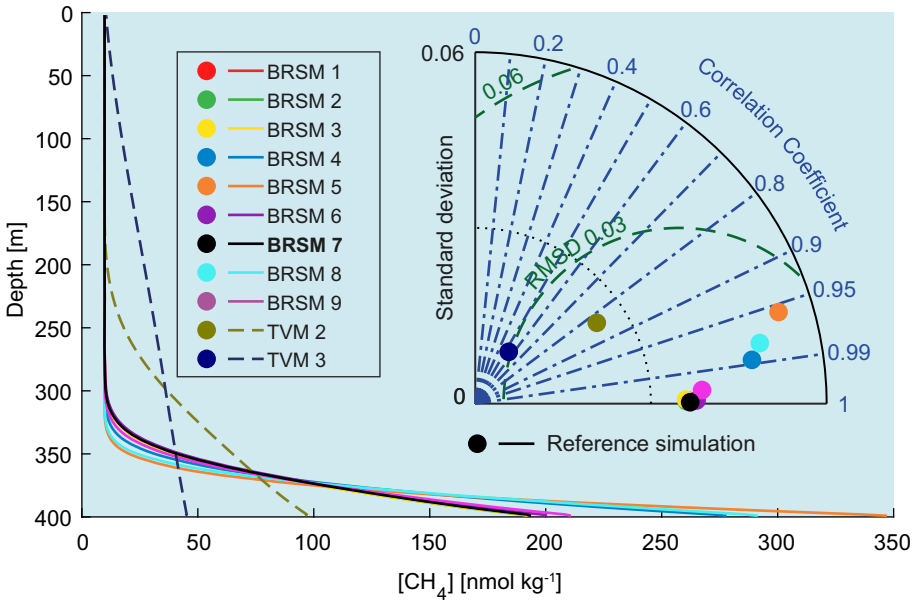

Fig. 4. Simulation results targeting BRSMs (solid lines) and TVMs (dashed lines). The main graph shows dissolved CH_4 concentration profiles in the water column after simulations reached steady state. Dots in the Taylor diagram (Taylor 2001) indicate standard deviation, correlation coefficients, and RMSD compared to the reference simulation (black line and dot) and are color coordinated with the profiles. The profile resulting from BRSM No. 3 was identical to the reference and is therefore hidden. The nine BRSM simulations use TVM No. 1, and the TVM simulations use BRSM No. 7.

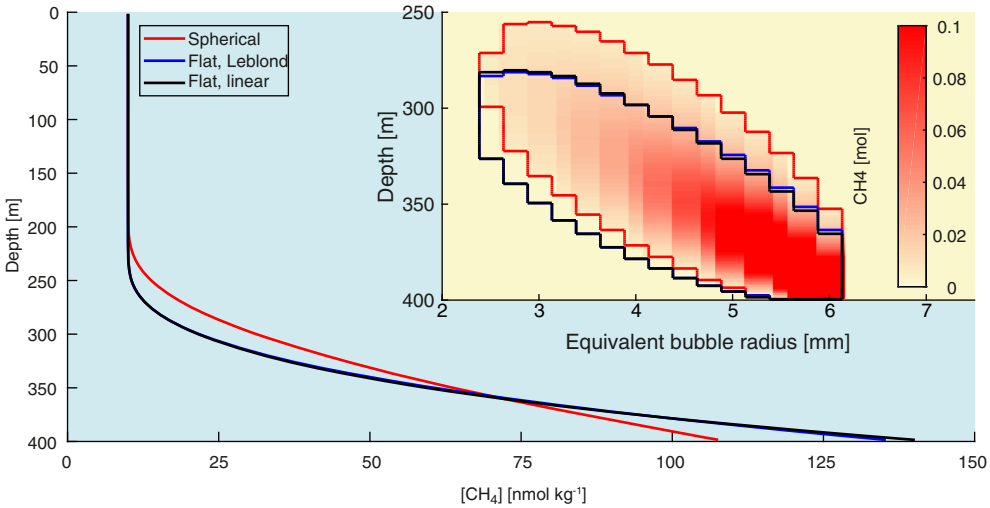

Fig. 5. Influence of flat bubble parameterizations. The main graph shows the steady-state profiles of dissolved CH_4 concentrations using initial r_E = 6 mm. The red line represents the simulation with spherical bubbles. Black and blue lines show results from linear and Leblond flatness parameterizations, respectively. The inset diagram shows free CH_4 gas content at steady state for the three simulations. Red color scale and bounding polygon indicate the spherical case while black and blue polygons represent Leblond and linear flatness parameterizations. Polygon boundaries were calculated from a 1-mmol free gas content threshold.

justifying a reference case based on a surfactant BRSM. Conversely, TVMs based on surfactant-covered bubbles yield unrealistic profiles, and we therefore chose a clean bubble TVM for the reference case.

We define the modeled flare height (equivalent to the acoustic signatures of free gas in the water column) as the height where less than a threshold fraction of the emitted gas remains. Here, we consider a 10% threshold, and we hereafter refer to the corresponding 10% flare height as FH10. The height of the modeled flares and consequently the vertical distribution of dissolved CH_4 in the water column are affected by the choice of BRSM. Simulations show that the FH10 is 41% higher when BRSM No. 9 is chosen compared to when BRSM No. 5 is applied, i.e., 51.6 vs. 36.6 m (Supporting Information Table S7), despite the fact that both models consider surfactant covered bubbles. The FH10s in the BRSM subgroup were 49.5 ± 6.4 m, and the concentration close to the seafloor in the present subgroup was 0.24 ± 0.06 μmol kg^{-1}, highlighting the importance of the choice of BRSM in the prediction of the vertical distribution of CH_4 in the water column.

Simulations using TVM for both semiclean (TVM No. 2) and surfactant (TVM No. 3) yielded strikingly different profiles compared to the reference case (TVM No. 1). Our simulations showed that bubbles rose more than twice as high compared to the reference case with a TVM based on intermediately surfactant-covered bubble rims. The FH10 of TVM No. 2 was 135.8 m compared to 54.6 m for the reference case (TVM No. 1). The surfactant based TVM (No. 3) caused bubbles to reach the surface even from 400 m water depth. Bubbles have not been observed to rise this high outside the hydrate stability zone (HSZ).

The importance of the bubble flatness parameterizations was investigated using single-size initial bubbles of r_E = 6 mm and otherwise default settings. One case was based on the linear flatness as previously described, which is also used in our reference case, a second case used the flatness parametrization suggested by Leblond et al. (2014), and the third case assumed spherical bubbles. These simulations showed that the FH10 was 21% higher when spherical bubbles were applied compared to the two flat bubble parameterizations, both of which showed similar results (Fig. 5). The dissolved CH_4 concentration profiles from these special cases had smaller gradients, and the maximum concentration (close to the seafloor) was 23% lower when spherical bubbles were assumed. For r_E= 3 bubbles, the FH10 resulting from the spherical bubble assumption was 5% lower than the flare height of flat bubbles (Supporting Information Table S8). The simple linear flatness parameterization produced similar results to the parameterization of Leblond while avoiding the sharp flatness transition at semimajor axis at 1.48 mm and is therefore recommended (Fig. 3a).

Model sensitivity to environmental conditions

We performed 41 simulations including the reference case with varying settings in order to evaluate the relative importance of environmental conditions (Table 1, subgroups 4–11) on the resulting vertical profile of dissolved CH_4. Fig. 6 shows an overview of the importance of the environmental parameters. The simulation results obtained from different conditions are summarized in Table SI.8 and the results are evaluated separately in the following sections. Definitions of the correlation coefficient, root mean square difference and standard deviations are provided in Supporting Information Table S8.

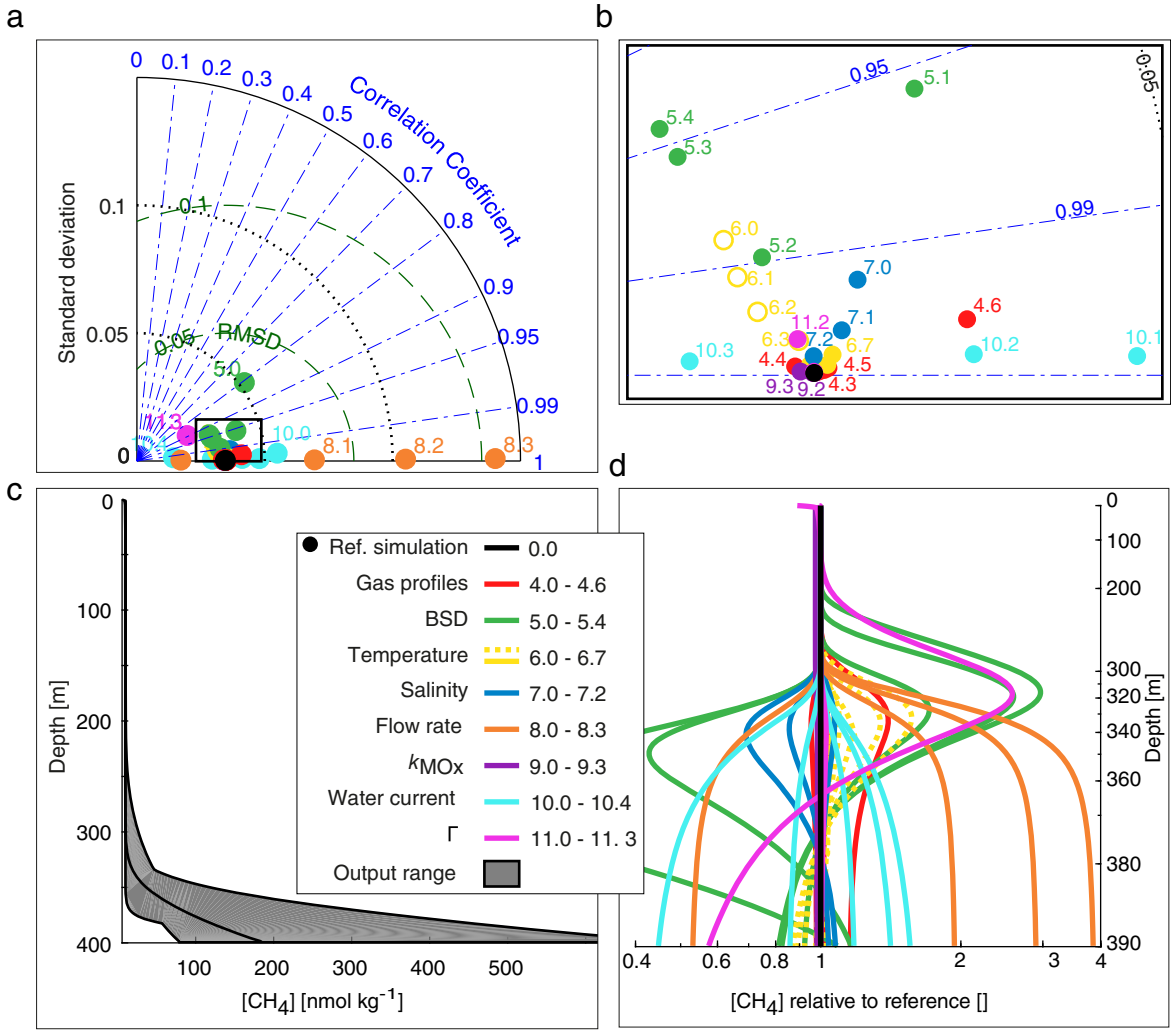

Fig. 6. Modeled CH_4 profiles and statistics. **(a)** Taylor diagram showing the standard deviation, RMSD, and correlation coefficient of simulations compared to the reference case, shown in black. Red dots, varying dissolved gas profiles; green dots, varying BSD; yellow dots, varying temperature; blue dots, varying salinity; orange dots, varying flow rates; purple dots, varying oxidation rate; light blue dots, varying water current; and pink dots, varying vertical mixing. **(b)** Zoom of the black rectangle in panel **a**, with the same color coding. **(c)** Dissolved gas vertical profiles after simulations reached steady state. Gray area shows the span of the model output for all simulations with varying environmental aspects. The reference simulation is shown as a black line. **(d)** Steady-state profiles following the same color coding, normalized by the reference case profile and plotted on a logarithmic depth axis. Dashed (yellow) lines indicate simulations partly within the CH_4-HSZ (see Supporting Information Table S8 for details). Simulations 11.0 and 11.1 are not seen here because they coincide with the reference simulation. Note the different depth scales of panels **c** and **d** for a more detailed visualization.

Dissolved gas profiles

We ran seven simulations using different gas profiles (simulations 4.0–6; Table 1 and Supporting Information Table S8 for details; red dots and lines in Fig. 6). Small deviations from the reference case simulation result from changing the ambient dissolved gas profiles. Neither removing the Argon gas, accounting for approximately 1% of the atmospheric gas composition, nor reducing the oxygen concentration by 99% changed the rise height of the CH_4 plume. An improbable 10-fold increase in N_2 increased the FH10 by 13 m. Simulations suggest that the initial and boundary dissolved gas concentrations within plausible ranges do not significantly influence the rise height of free gas in environments where the water mass is well-ventilated like in all our cases.

Bubble size distribution

An important feature of M2PG1 is its capability to simulate bubbles with a range of bubbles sizes, which is typically observed in natural seep systems. However, in order to isolate the effect of different bubble sizes, it was necessary to simplify the size distribution and simulate the release of bubbles, of initially one size. Five single-size bubble simulations were performed (simulations 5.0–4; r_E = [1, 2, 4, 6, 8] mm; green dots and lines in Fig. 6), which showed that the size of

bubbles escaping from the seafloor strongly affects the vertical distribution of dissolved CH_4. Compared to 3 mm bubbles (our reference), the 10% CH_4 plume was lower by 57% when r_E = 1 mm was assumed and was higher by 87% for r_E = 8 mm. Small bubbles have the capacity to increase the near-seafloor concentration because they dissolve quickly and rise slowly. For example, the bottom water CH_4 concentration was 230% higher with r_E = 1 mm bubbles than with r_E = 3 mm bubbles.

Temperature

Simulations using eight vertically homogenous temperature profiles (simulations 6.0–7; $T \in$ [0, 1, 2, 3, 6, 8, 10, 20]°C) are shown as yellow dots and lines in Fig. 6. Bubbles within the HSZ become covered with hydrate skins (e.g., Sauter et al. 2006), but the growth rate of hydrates on bubble rims and their influence on the gas transfer velocity and rising speed are largely unknown and therefore not implemented in this version of M2PG1. Simulations 6.0–6.3 with temperatures, $T \in$ [0, 1, 2, 3]°C, are partly within the HSZ and therefore unreliable. To isolate the temperature effect on bubble dynamics, we performed an additional 18 simulations (not shown in Table 1 or Supporting Information Table S8) with the release of CH_4 bubbles from 100 and 200 m water depths, where CH_4 hydrates are unstable at all temperatures. We observe a weak trend toward higher plume heights with higher temperatures (Fig. 7), to which we attribute the lower solubility associated with warmer water.

Salinity

Simulations using three different vertically homogenous salinity profiles (simulations 7.0–2; PSU ∈ [0, 20, 40]; blue dots and lines in Fig. 6) confirm that high salinity causes gas to rise higher. The 40 PSU salinity causes the CH_4 plume to reach 12% higher compared to the 20 PSU case and 21% higher compared to the freshwater case. This is explained by the lower solubility of CH_4 caused by salts in the water. The plume height difference between the 35 PSU case and the freshwater case was 12 m (14%).

Flow rate

Any change in flow rate (simulations 8.0–3; $Q_{EF} \in$ [0.025, 0.1, 0.15, 0.2] mol s^{-1}; orange dots and lines in Fig. 6) simply resulted in absolute concentration shifts. The shape of the dissolved CH_4 profiles did not change due to changed flow rates. This stems from the fact that the modeling approach does not consider bubble–bubble interaction or upwelling flow caused by bubbles.

Aerobic CH_4 oxidation rate constant (k_{MOX})

Five different simulations, using different values of k_{MOX} (simulations 9.0–3; $k_{MOX} \in$ [0, 0.01, 0.1, 1, 10] d^{-1}) yield profiles with a near-perfect match. This implies that aerobic oxidation of CH_4 is negligible on time scales given by relatively strong water currents and small domain sizes: in the simulations, we consider a domain of 1800 m^2, equal to the echosounder beam area of 25 m radius, and a default water current of 15 cm s^{-1}, yielding a residence time of 5 min, which for k_{MOX} = 1 d^{-1} would remove less than 5‰ of the present CH_4.

Water currents

Five simulations addressing the effect of advection through ocean currents (simulations 10.0–4; $u \in$ [2.5, 5, 10, 20, 50] cm s^{-1}; cyan dots in Fig. 6) were performed. The profiles of all state variables at the lateral boundary were vertically homogenous throughout our sensitivity simulations, and the inflow of dissolved gas

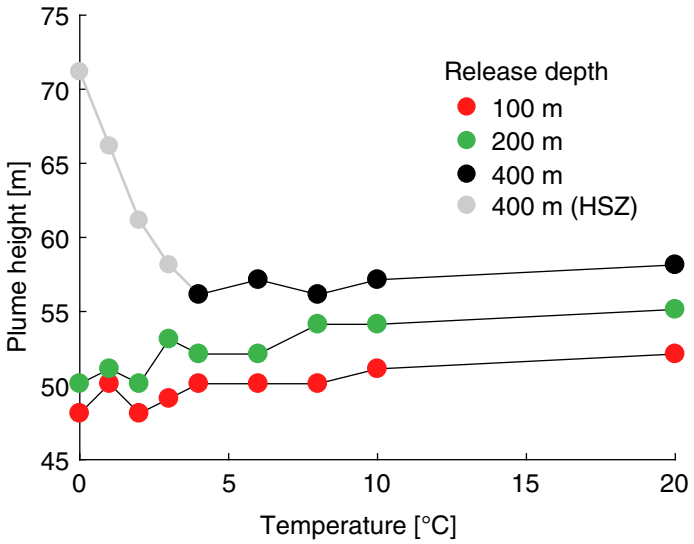

Fig. 7. Temperature-dependent dissolved CH_4 plume heights. Plume heights are calculated as the height where the concentration anomaly is less than 10% of the maximum anomaly. Red, green, and black dots represent plume heights from bubbles released at 100, 200, and 400 m, respectively. Gray dots indicate that the bubbles are partly within the CH_4-HSZ and therefore represent unrealistic results.

nudged the concentration profiles toward the boundary level. Therefore, profiles resulting from strong currents were more similar to the boundary profiles. Specifically, CH_4 profiles displayed smaller gradients and lower concentrations for cases with stronger currents. Plume heights were higher for stronger water currents but not higher by absolute concentrations (Supporting Information Table S8). This is consistent with the fact that the ambient concentrations did not affect the bubble rise heights significantly.

Vertical mixing

Wunsch and Ferrari (2004) reported on oceanic vertical diffusion coefficients ranging from 3×10^{-4}–500×10^{-4} m^2 s^{-1}. A plausible low eddy diffusion coefficient (simulation 11.0; 10^{-4} m^2 s^{-1}) did not influence the vertical distribution of dissolved CH_4 and neither did a high coefficient (simulation 11.1; $\Gamma = 1$ m^2 s^{-1}). A mixing coefficient of 100 m^2 s^{-1}, represented by the pink dot (11.2) and hardly visible pink line in Fig. 6, only slightly changed the profile. The vertical profile was noticeably altered by the high-end mixing coefficient (simulation 11.3; $\Gamma = 10^4$ m^2 s^{-1}), but such strong vertical mixing is not observed in the ocean. The vertical mixing of dissolved gas is thus negligible in environments where ocean currents carry the dissolved methane away from the source. The fate of seeped methane is only marginally dependent on vertical mixing even away from the source area (Graves et al. 2015) unless turbulence is particularly enhanced.

Case study

We performed a 3-d ship-based survey at a known CH_4 seepage site (e.g., Westbrook et al. 2008; Sahling et al. 2014) on the

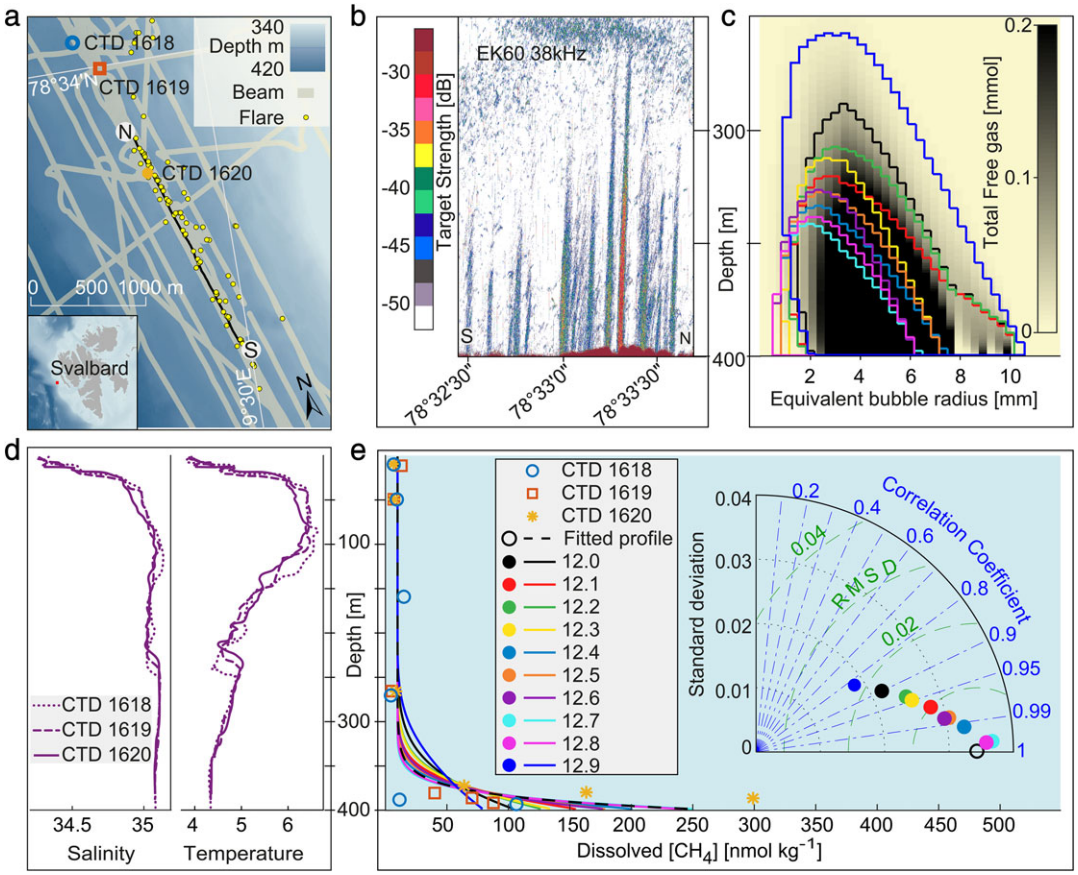

Fig. 8. Case study compared to model simulations. **(a)** Map of the case study area showing identified flares (yellow dots), echosounder beam coverage (gray lines), the transect shown in panel **b** (black line delimited by labels S and N), and CTD cast locations (blue ring [CTD 1618], red square [CTD 1619], and orange star [CTD 1620], referred to in panels **d** and **e**). **(b)** Echosounder data acquired from the ship mounted EK60 operated at 38 kHz on 22 October, following the track from S to N in panel **a**. Colors indicate the target strength (dB)—an indicator for the quantity of free gas (bubbles) in the water. **(c)** Gray to black shades indicates the modeled content of free gas (all species) at steady state of simulation 12.0 and its distribution in bubble size and depth bins. Colored contour lines indicate the limit where the free gas exceeds 0.05 mmol. Contours for model simulations are color coded accordingly with the legend in panel **e**. **(d)** Salinity and temperature profiles of performed CTD casts. **(e)** Discrete CH_4 concentrations acquired from CTD casts and subsequent gas chromatograph measurements shown with symbols matching panel **a**. A continuous dissolved CH_4 profile function, fitted to the discrete data, is shown as a dashed black line. Steady-state model output profiles are shown as lines with the same color coding as panel **c**. Inset Taylor diagram summarizes the correlation coefficient, standard deviation, and RMSD between the fitted profile and the model simulations (equations in Supporting Information Table S7). Dots in the Taylor diagram are color coded accordingly with the legend.

continental slope west of Svalbard in October 2015 (Fig. 8a), where we acquired continuous echosounder data (EK60 operated at 18 and 38 kHz). Bubble streams, inferred from the echosounder data were observed to rise 50–150 m above the seafloor. We performed three conductivity-temperature-depth (CTD) hydrocasts including discrete water samples in the close vicinity of gas flares (Fig. 8a for locations). Water samples were analyzed for aqueous CH_4 concentrations following the headspace gas chromatography method described by Magen et al. (2014). A continuous exponential function was fitted to the discrete CH_4 concentration data and was subsequently used for comparison with model simulations (Fig. 8e).

We performed 10 simulations using the temperature and salinity data from the three CTD casts (Fig. 8d) as boundary conditions. For simulations 12.0–12.2, we used a Gaussian-like BSD peaking at r_E = 3 mm, which was observed in the area in 2011 and 2012 (Veloso et al. 2015). Simulations 12.3–12.5 were set up with smaller bubbles (peak radius of 2 mm) and 12.6–12.8 were set up with 1 mm peak radius. Simulation 12.9 used a 6 mm peak radius. The water current was estimated to 18.5 cm s^{-1} based on the inclination of flare spines calculated with the FlareHunter software (Veloso et al. 2015). BRSM No. 7 was used in simulations 12.0, 12.3, and 12.6; BRSM No. 5 was used in 12.1, 12.4, and 12.7; BRSM No. 8 was used in 12.2, 12.5, 12.8, and 12.9.

We calculated backscatter areas and target strength (TS) values from the case study simulations according to eqs. 1–9 in Veloso et al. (2015), after the model reached steady state. We defined a TS height as the height where the simulated TS dropped below −55 dB (value used for discriminating between gas and water). The resulting TS heights were 69–134 m above the seafloor for the included cases.

The observed acoustic flare heights (Fig. 8b) were well-reproduced by the 10 case study simulations (Fig. 8c and Supporting Information Table S7): The TS height obtained with simulation 12.9, using a 6 mm peak radius BSD, matched the highest observed flares, whereas the heights obtained from simulations 12.0–12.8, using smaller BSDs matched the height of the lower flares (Fig. 8b,c). Simulated dissolved CH_4 profiles correlated well ($r > 0.9$) with the fitted function and the root-mean-square difference (RMSD) was less than 0.02 μmol kg^{-1}. The simulations using 3 mm peak radius bubbles show that the modeled dissolved CH_4 concentrations near the seafloor were lower than the concentrations of the fitted curve, but above approximately 15 m, the simulated concentrations were higher (Fig. 8e). The small bubble simulations (12.7 and 12.8) produced dissolved methane profiles almost identical with the fitted function based on observations.

Discussion and conclusion

We developed a M2PG1 that simulates the dynamics of free and dissolved gases in the water column. To our knowledge, it is the first model that simulates the two gas phases simultaneously, with multiple bubble sizes comprising multiple gases. M2PG1 considers nonideal gas behavior, pressure-, temperature-, and salinity-dependent solubility and diffusivity. M2PG1 resolves direct bubble-mediated gas escape to the atmosphere as well as diffusive flow of dissolved gas through equilibration with the atmosphere. The model also simulates aerobic oxidation, converting CH_4 into carbon dioxide while consuming oxygen. The numerical accuracy of the model was better than 99.9% which, in spite of the more complex calculations, is comparable with the model developed by Vielstädte et al. (2015). Predicting the fate of bubble gas in the water column requires knowledge of the sizes and gas composition of the bubbles, water currents, and initial and boundary conditions of salinity, temperature, and dissolved gas species. Moreover, parameterizations of bubble shapes, rising speeds, and transfer velocities must be applied. We performed 12 simulations to estimate the importance of technical model settings and another 40 simulations to assess the importance of environmental conditions. We also compared a case of CH_4 gas emission from the seafloor west of Svalbard with simulations.

Technical parameters

Bubble shapes are implicitly considered in the rising speed parameterizations, but experiments determining the gas transfer velocities have not addressed bubble shapes and the increased bubble surface of nonspherical bubbles. This analysis showed that applying flat bubble parameterizations reduced the rise height of gas by 22% for 6 mm bubbles and by 5% for 3 mm bubbles. TVM No. 3, based on surfactant-covered bubbles, increased the flare height so much that bubbles reached the surface even in our 400-m deep model. Such high bubble streams are not observed in an environment outside the CH_4 hydrate stability field. Clean bubble TVM simulations produced dissolved CH_4 profiles well correlated ($r \geq 0.90$) with CH_4-profiles observed during the CAGE 15-6 cruise. As the other applied TVMs resulted in deviating CH_4 profiles, we suggest that, for future simulations of Arctic seafloor emissions of CH_4 bubbles, a clean bubble TVM should be used.

Environmental parameters

Varying ambient dissolved gas profiles have little effect on the resulting CH_4 profiles. Only an unlikely 10-fold increase of nitrogen noticeably altered the rise-height of CH_4 and neglecting dissolved argon gas has no effect on the resulting profiles. Consequently, we suggest that M2PG1 users may assume that dissolved gases are initially in equilibrium with the atmosphere. The resulting vertical distribution of dissolved CH_4 is highly dependent on the initial bubble size and plume heights are roughly 60% lower when using small bubbles and 90% higher when large bubbles are assumed. We therefore stress the importance of acquiring in situ BSDs. High salinity causes bubbles to rise higher due to the lower solubility in saline water, but the response in flare height caused by temperature is limited to a few meters. Simulations show that both MOX and vertical mixing within plausible ranges can be neglected in a seepage region

with high water velocity. However, MOX and vertical mixing may still be important for the fate of CH_4 away from the sources on ocean basin scales. The *e*-folding oxidation time scale (the time it takes before the bulk of the CH_4 is removed by oxidation) is $1/k_{MOX}$: 100 d for our reference simulation and 2.4 h for simulation 9.3 with extremely fast removal rate.

Model comparison with observations

M2PG1 reproduced well ($r > 0.9$ and RMSD < 0.02 μmol kg^{-1}) the observed dissolved CH_4 profiles acquired during the CAGE 15-6 cruise, using the BSD observed in the area in 2011 and 2012. Ideally, the simulated profile shapes should have a sharper decrease upward. Such profiles resulted from simulations using smaller initial bubble sizes. Simulated free gas reached heights consistent with most of the flares seen in the echograms acquired during the same research cruise. However, the most prominent flares, reaching over 150 m above the seafloor, were higher than the model simulations (12.0–12.8) predicted. This could be attributed to larger bubble sizes or upwelling caused by intense bubble release. The CTD data do not show enough evidence for upwelling to explain the highest flares: The density stratification was neutral or unstable only at Sta. 1619 and 1620 between 0 and 20 m above the seafloor (the buoyancy frequency was only slightly imaginary: $N^2 \in [-0.5 \times 10^{-6}, 0]$). However, when larger initial bubble sizes were applied (simulation 12.9 uses a Gaussian BSD peaking at 6 mm), the flare reaches up to 167 m above the seafloor, which matches the highest observed flares. We therefore explain the highest flares by the presence of bubbles larger than observed, rather than by local upwelling.

Future use and developments

M2PG1 resolves free and dissolved gas dynamics in shallow to moderately deep aquatic environments, and the depth limitation is currently given by the depth of the pressure-, temperature-, and salinity-dependent HSZs. In order to apply the model at deeper sites, including depths within the HSZs, future versions of M2PG1 should include TVMs and BRSMs for hydrate-coated bubbles and possibly model growth and dissociation of hydrates on bubble skins and the subsequent effect on gas transfer and bubble rising speeds.

Our study indicates that bubble streams with large bubbles (simulations 5.4 and 12.9) could reach as high as 170 m and 10% of the emitted CH_4 may reach up to 100 m. If such emissions occur at shallow seep sites and/or vertical mixing is particularly enhanced due to surface water cooling or storms (winter mixing), some of the CH_4 will ultimately reach the atmosphere. Long-term simulations forced with transient and realistic boundary conditions such as temperature, salinity, aqueous gas concentrations, mixing coefficients, wind speed, and water currents would be required to quantify this effect.

The application of M2PG1 targeting methane seepage from the seafloor provides a well-structured basis for future incorporation in ocean models with horizontal resolution. For example, the Svalbard 800 model (Hattermann et al. 2016) could easily be coupled with M2PG1. Alternatively, PROBE's capability of coupling ocean basins may be used. This kind of model combination would allow for prediction of spatial and temporal distribution of CH_4 emission to the atmosphere.

Future versions of M2PG1 could potentially include the carbonate system (e.g., Liang et al. 2011; Edman and Omstedt 2013), which would allow for direct simulation of ocean acidification caused by CH_4 seeps.

In order to predict the vertical distribution of gas at sites where bubble emission is very intense, bubble-driven upwelling could be incorporated, and may be predicted from the number density and drag of buoyant bubbles on the water. Newly developed acoustic instruments providing broadband signals could facilitate determination of bubble sizes by inverse acoustic modeling of BSD by remote methods. This would greatly simplify the determination of BSDs, which is important for predicting the vertical distribution of CH_4 emitted from the seafloor.

Although the main interest of this study was related to CH_4, a consequence of the coupled gas system is that, once a process-based model is established, it inevitably provides insight to the evolution of all the present gas species, both in their free and dissolved phases. For example, redistribution of dissolved CO_2 and O_2 due to CH_4 bubbles can be assessed. The effect of bubbles injected to surface waters by wave action and the fate of gas leakage from industrial seafloor installations can be understood from the same process-based model.

Data availability statement

A dataset comprising the executable file, simulation settings, and results was deposited in the UiT Open Research Data repository https://doi.org/10.18710/LS2KUX.

References

Al Zaitone, B. 2018. Evaporation of oblate spheroidal droplets: A theoretical analysis. Chem. Eng. Commun. **205**: 110–121. doi:10.1080/00986445.2017.1374949

Angelis, M. A., and M. I. Scranton. 1993. Fate of methane in the Hudson River and estuary. Global Biogeochem. Cycles **7**: 509–523. doi:10.1029/93GB01636

Biastoch, A., and others. 2011. Rising Arctic Ocean temperatures cause gas hydrate destabilization and ocean acidification. Geophys. Res. Lett. **38**: 38. doi:10.1029/2011GL047222

Blanchard, D. C. 1989. The ejection of drops from the sea and their enrichment with bacteria and other materials: A review. Estuaries **12**: 127–137. doi:10.2307/1351816

Boetius, A., and F. Wenzhöfer. 2013. Seafloor oxygen consumption fuelled by methane from cold seeps. Nat. Geosci. **6**: 725–734. doi:10.1038/ngeo1926

Carlsson, B., A. Rutgersson, and A.-S. Smedman. 2009. Investigating the effect of a wave-dependent momentum flux in a

process oriented ocean model. Boreal Environ. Res. **14**: 1543–1554. doi:10.1007/s11274-015-1903-5

Collins, G. L., M. Motarjemi, and G. J. Jameson. 1978. A method for measuring the charge on small gas bubbles. J. Colloid Interface Sci. **63**: 69–75. doi:10.1016/0021-9797(78)90036-X

Damm, E., A. Mackensen, G. Budéus, E. Faber, and C. Hanfland. 2005. Pathways of methane in seawater: Plume spreading in an Arctic shelf environment (SW-Spitsbergen). Cont. Shelf Res. **25**: 1453–1472. doi:10.1016/j.csr.2005.03.003

Delnoij, E., F. Lammers, J. Kuipers, and W. Van Swaaij. 1997. Dynamic simulation of dispersed gas-liquid two-phase flow using a discrete bubble model. Chem. Eng. Sci. **52**: 1429–1458. doi:10.1016/S0009-2509(96)00515-5

Edenhofer, O., and others. 2014. IPCC, 2014: Summary for policymakers. Mitigation of climate change. Cambridge University Press.

Edman, M., and A. Omstedt. 2013. Modeling the dissolved CO_2 system in the redox environment of the Baltic Sea. Limnol. Oceanogr. **58**: 74–92. doi:10.4319/lo.2013.58.1.0074

Ferré, B., J. Mienert, and T. Feseker. 2012. Ocean temperature variability for the past 60 years on the Norwegian-Svalbard margin influences gas hydrate stability on human time scales. J. Geophys. Res.: Oceans **117**: C10017. doi:10.1029/2012JC008300

Fofonoff, N. 1985. Physical properties of seawater: A new salinity scale and equation of state for seawater. J. Geophys. Res.: Oceans **90**: 3332–3342. doi:10.1029/JC090iC02p03332

Graves, C. A., and others. 2015. Fluxes and fate of dissolved methane released at the seafloor at the landward limit of the gas hydrate stability zone offshore western Svalbard. J. Geophys. Res.: Oceans **120**: 6185–6201. doi:10.1002/2015JC011084

Gustafsson, N., L. Nyberg, and A. Omstedt. 1998. Coupling of a high-resolution atmospheric model and an ocean model for the Baltic Sea. Mon. Weather Rev. **126**: 2822–2846. doi:10.1175/1520-0493(1998)126%3C2822:COAHRA%3E2.0.CO;2

Hansson, D., and A. Omstedt. 2008. Modelling the Baltic Sea ocean climate on centennial time scale: Temperature and sea ice. Clim. Dyn. **30**: 763–778. doi:10.1007/s00382-007-0321-2

Hattermann, T., P. E. Isachsen, W. J. Appen, J. Albretsen, and A. Sundfjord. 2016. Eddy-driven recirculation of Atlantic water in Fram Strait. Geophys. Res. Lett. **43**: 3406–3414. doi:10.1002/2016GL068323

Jähne, B., K. O. Münnich, R. Bösinger, A. Dutzi, W. Huber, and P. Libner. 1987. On the parameters influencing air-water gas exchange. J. Geophys. Res.: Oceans **92**: 1937-1949. doi:10.1029/JC092iC02p01937

Johansen, Ø. 2000. DeepBlow—a Lagrangian plume model for deep water blowouts. Spill Sci. Technol. Bull. **6**: 103–111. doi:10.1016/S1353-2561(00)00042-6

Kirschke, S., and others. 2013. Three decades of global methane sources and sinks. Nat. Geosci. **6**: 813–823. doi:10.1038/ngeo1955

Leblond, I., C. Scalabrin, and L. Berger. 2014. Acoustic monitoring of gas emissions from the seafloor. Part I: Quantifying the volumetric flow of bubbles. Mar. Geophys. Res. **35**: 191–210. doi:10.1007/s11001-014-9223-y

Leifer, I., J. F. Clark, and R. F. Chen. 2000. Modifications of the local environment by natural marine hydrocarbon seeps. Geophys. Res. Lett. **27**: 3711–3714. doi:10.1029/2000GL011619

Leifer, I., and R. K. Patro. 2002. The bubble mechanism for methane transport from the shallow sea bed to the surface: A review and sensitivity study. Cont. Shelf Res. **22**: 2409–2428. doi:10.1016/S0278-4343(02)00065-1

Liang, J. H., J. C. McWilliams, P. P. Sullivan, and B. Baschek. 2011. Modeling bubbles and dissolved gases in the ocean. J. Geophys. Res.: Oceans **116**: C03015. doi:10.1029/2010JC006579

Luff, R., K. Wallmann, and G. Aloisi. 2004. Numerical modeling of carbonate crust formation at cold vent sites: Significance for fluid and methane budgets and chemosynthetic biological communities. Earth Planet. Sci. Lett. **221**: 337–353. doi:10.1016/S0012-821X(04)00107-4

Magen, C., L. L. Lapham, J. W. Pohlman, K. Marshall, S. Bosman, M. Casso, and J. P. Chanton. 2014. A simple headspace equilibration method for measuring dissolved methane. Limnol. Oceanogr.: Methods **12**: 637–650. doi:10.4319/lom.2014.12.637

Mau, S., and others. 2017. Widespread methane seepage along the continental margin off Svalbard-from Bjørnøya to Kongsfjorden. Sci. Rep. **7**: 42997. doi:10.1038/srep42997

McGinnis, D., J. Greinert, Y. Artemov, S. Beaubien, and A. Wüest. 2006. Fate of rising methane bubbles in stratified waters: How much methane reaches the atmosphere? J. Geophys. Res.: Oceans (1978–2012) **111**: C09007. doi:10.1029/2005JC003183

Myhre, C. L., and others. 2016. Extensive release of methane from Arctic seabed west of Svalbard during summer 2014 does not influence the atmosphere. Geophys. Res. Lett. **43**: 4624–4631. doi:10.1002/2016GL068999

Omstedt, A. 2011. Guide to process based modeling of lakes and coastal seas. Springer.

Omstedt, A., and J. S. Wettlaufer. 1992. Ice growth and oceanic heat flux: Models and measurements. J. Geophys. Res.: Oceans **97**: 9383–9390. doi:10.1029/92JC00815

Pachauri, R. K., and others. 2014. Climate change 2014: Synthesis report. Contribution of Working Groups I, II and III to the fifth assessment report of the Intergovernmental Panel on Climate Change. IPCC.

Panieri, G., and others. 2017. An integrated view of the methane system in the pockmarks at Vestnesa Ridge, 79°N. Mar. Geol. **390**: 282–300. doi:10.1016/j.margeo.2017.06.006

Randelhoff, A., A. Sundfjord, and M. Reigstad. 2015. Seasonal variability and fluxes of nitrate in the surface waters over the Arctic shelf slope. Geophys. Res. Lett. **42**: 3442–3449. doi:10.1002/2015GL063655

Rehder, G., P. W. Brewer, E. T. Peltzer, and G. Friederich. 2002. Enhanced lifetime of methane bubble streams within

the deep ocean. Geophys. Res. Lett. **29**: 21-1–21-4. doi:10.1029/2001GL013966

Ruppel, C. D., and J. D. Kessler. 2016. The interaction of climate change and methane hydrates. Rev. Geophys. **55**: 126–168. doi:10.1002/2016RG000534

Sahling, H., and others. 2014. Gas emissions at the continental margin west of Svalbard: Mapping, sampling, and quantification. Biogeosciences **11**: 6029–6046. doi:10.5194/bg-11-6029-2014

Sam, A., C. Gomez, and J. Finch. 1996. Axial velocity profiles of single bubbles in water/frother solutions. Int. J. Miner. Process. **47**: 177–196. doi:10.1016/0301-7516(95)00088-7

Sauter, E. J., and others. 2006. Methane discharge from a deep-sea submarine mud volcano into the upper water column by gas hydrate-coated methane bubbles. Earth Planet. Sci. Lett. **243**: 354–365. doi:10.1016/j.epsl.2006.01.041

Shakhova, N., I. Semiletov, A. Salyuk, V. Yusupov, D. Kosmach, and Ö. Gustafsson. 2010. Extensive methane venting to the atmosphere from sediments of the east Siberian Arctic shelf. Science **327**: 1246–1250. doi:10.1126/science.1182221

Shakhova, N., and others. 2014. Ebullition and storm-induced methane release from the east Siberian Arctic shelf. Nat. Geosci. **7**: 64–70. doi:10.1038/ngeo2007

Sloan, E. D., and C. Koh. 2007. Clathrate hydrates of natural gases. CRC Press.

Stepanenko, V. M., E. E. Machul'skaya, M. V. Glagolev, and V. N. Lykossov. 2011. Numerical modeling of methane emissions from lakes in the permafrost zone. Izv. Atmos. Oceanic Phys. **47**: 252–264. doi:10.1134/s0001433811020113

Svensson, U. 1978. A mathematical model of the seasonal thermocline. Elsevier.

Svensson, U., and A. Omstedt. 1998. Numerical simulations of frazil ice dynamics in the upper layers of the ocean. Cold Reg. Sci. Technol. **28**: 29–44. doi:10.1016/S0165-232X(98)00011-1

Taylor, K. E. 2001. Summarizing multiple aspects of model performance in a single diagram. J. Geophys. Res.: Atmos. **106**: 7183–7192. doi:10.1029/2000JD900719

Thorpe, S. A. 2007. An introduction to ocean turbulence. Cambridge University Press.

Uhlig, C., and B. Loose. 2017. Using stable isotopes and gas concentrations for independent constraints on microbial methane oxidation at Arctic Ocean temperatures. Limnol. Oceanogr.: Methods **15**: 737–751. doi:10.1002/lom3.10199

Valentine, D. L., D. C. Blanton, W. S. Reeburgh, and M. Kastner. 2001. Water column methane oxidation adjacent to an area of active hydrate dissociation, Eel River basin. Geochim. Cosmochim. Acta **65**: 2633–2640. doi:10.1016/S0016-7037(01)00625-1

Veloso, M., J. Greinert, J. Mienert, and M. De Batist. 2015. A new methodology for quantifying bubble flow rates in deep water using splitbeam echosounders: Examples from the Arctic offshore NW-Svalbard. Limnol. Oceanogr.: Methods **13**: 267–287. doi:10.1002/lom3.10024

Vielstädte, L., . 2015. Quantification of methane emissions at abandoned gas wells in the Central North Sea. Mar. Pet. Geol. **68:** 848–860. doi:10.1016/j.marpetgeo.2015.07.030

Wanninkhof, R. 1992. Relationship between wind speed and gas exchange over the ocean. J. Geophys. Res.: Oceans (1978–2012) **97:** 7373–7382, doi:10.1029/92JC00188

Wanninkhof, R. 2014. Relationship between wind speed and gas exchange over the ocean revisited. Limnol. Oceanogr.: Methods **12**: 351–362. doi:10.4319/lom.2014.12.351

Westbrook, G. K., and others. 2008. Estimation of gas hydrate concentration from multi-component seismic data at sites on the continental margins of NW Svalbard and the Storegga region of Norway. Mar. Pet. Geol. **25**: 744–758. doi:10.1016/j.marpetgeo.2008.02.003

Westbrook, G. K., and others. 2009. Escape of methane gas from the seabed along the West Spitsbergen continental margin. Geophys. Res. Lett. **36**: L15608. doi:10.1029/2009GL039191

Woolf, D. K. 1993. Bubbles and the air-sea transfer velocity of gases. Atmos. Ocean **31**: 517–540. doi:10.1080/07055900.1993.9649484

Wunsch, C., and R. Ferrari. 2004. Vertical mixing, energy, and the general circulation of the oceans. Annu. Rev. Fluid Mech. **36**: 281–314. doi:10.1146/annurev.fluid.36.050802.122121

Zheng, L., and P. D. Yapa. 2002. Modeling gas dissolution in Deepwater oil/gas spills. J. Mar. Syst. **31**: 299–309. doi:10.1016/S0924-7963(01)00067-7

Acknowledgments

This work was supported by the Research Council of Norway through its Centres of Excellence funding scheme, project number 223259. We would like to thank the crew on board RV *Helmer Hanssen* for the support during the CAGE 15-6 cruise and the cruise leader Jürgen Mienert.

Conflict of Interest

None declared.

Submitted 04 October 2018
Revised 13 December 2018
Accepted 18 December 2018

Associate editor: Mike DeGrandpre